

The Atomic Structure of Ultrathin Oxide Films and Interfaces Studied by Surface X-Ray Diffraction

Katayoon Mohseni and Holger L. Meyerheim*

X-ray diffraction (XRD) studies of the atomic structure of ultrathin oxide films and interfaces are presented, which are conducted within the framework of the Sonderforschungsbereich 762 (functionality of oxide interfaces). Knowledge of the atomic structure is at the heart of the study of functional oxides. XRD allows the investigation of complex systems frequently encountered in oxide systems (large unit cells, complex relaxation patterns, and structural and chemical disorder). Results are combined with first-principles calculations and complementary techniques providing a thorough understanding of the oxides' functionality. The structure analysis of the approximant (AP) to the 2D oxidic quasicrystal (QC) based on BaTiO_3 (BTO) is discussed, the first oxide-type QC discovered. This AP is related to the Kepler tiling described 400 years ago. The $\text{LaFeO}_3/\text{SrTiO}_3$ interface is examined, which is a prototype for the formation of a 2D electron gas (2DEG). Subtle interfacial chemical roughness in combination with oxygen off-stoichiometry strongly influences the critical LaFeO_3 thickness for the 2DEG formation. Finally, the analysis of the multiferroic BTO/ME(001) (ME = Fe, Pd, Pt) interface reveals that a submonolayer of impurities is the origin for the inversion of the BTO film/vacuum termination from BaO on Fe(001) to TiO_2 on Pt(001).

1. Introduction

Ultrathin oxide films and their interfaces have attracted intense interest for their outstanding structural and physical properties which have the potential to serve as functional materials in oxide-type electronics.^[1] Examples are systems in which the interface between the oxide and metal (ME) or between two oxides involves new functionalities. Prototypes are tunneling junctions involving an insulating oxide between two ferromagnetic metallic electrodes or interfaces between two insulating oxides. In the former case, special attention has been paid to the study of multiferroic systems where the insulating oxide barrier is a ferroelectric. In


this way, new functionalities arise by the possibility to switch both, the (relative) magnetization direction of the (ferromagnetic) electrodes and the polarization direction of the ferroelectric barrier.^[2,3] Beginning with early theoretical studies more than a decade ago,^[4–6] significant progress has been achieved in recent years, providing experimental evidence for the basic functionality of such devices. Nevertheless, a detailed microscopic understanding of the multiferroic effect is far from being complete, whereas it is becoming evident that the interface models used for theoretical modeling are too simplified in general. Thus, detailed investigations of the interface and film structures are highly demanded.

Similarly, the search for a thorough understanding as to why a 2D electron gas (2DEG) is formed^[7] at the interface between two insulating oxides such as between LaAlO_3 (LAO) and SrTiO_3 (STO) has made considerable progress, and several models which account for the onset

of the interface metallicity are discussed. The first one proposes the so-called “polarization catastrophe” in relation to an electronic reconstruction at the interface,^[8] another model refers to extrinsic origins among which the formation of oxygen defects within the oxide films and chemical roughness at their interface are the most prominent ones.^[9,10] A clear-cut exploration of the mechanisms at work for 2D interface metallization also requires a very detailed model of the film and interface atomic structure.

The examples discussed earlier are representative of the complexity and versatility of oxide materials in the context of potential new oxide electronic devices, but oxides have also appeared in a branch in solid-state physics which so far has been limited almost exclusively to ME alloys, namely, the structure and physics of quasicrystals (QCs) and their approximants (APs). In 1984, the first observation of a QC was published,^[11] but it took until 2013 to discover an oxide QC (OQC), which, with respect to stoichiometry, is closely related to BaTiO_3 (BTO) and which was grown as a 2D monolayer on Pt(111).^[12] Here, the surface X-ray diffraction (SXRD) analysis in combination with scanning tunneling microscopy (STM) experiments of the closely related “Kepler” AP provided direct insight into the atomic structure of the tiling elements (occupied by titanium) and the precise determination of the barium and oxygen positions.^[13,14] Especially, the latter is of utmost importance as it represents a direct and independent proof for the involvement of oxygen into the QC structure.

Dr. K. Mohseni, Dr. H. L. Meyerheim
Experimental Department IIV
Max-Planck-Institut für Mikrostrukturphysik Halle
Weinberg 2, D-06120 Halle, Germany
E-mail: holger.meyerheim@mpi-halle.mpg.de

 The ORCID identification number(s) for the author(s) of this article can be found under <https://doi.org/10.1002/pssb.201900605>.

© 2019 The Authors. Published by WILEY-VCH Verlag GmbH & Co. KGaA, Weinheim. This is an open access article under the terms of the Creative Commons Attribution License, which permits use, distribution and reproduction in any medium, provided the original work is properly cited.

DOI: 10.1002/pssb.201900605

This Feature Article presents several studies which have been conducted in project A5 during the period of the Sonderforschungsbereich (SFB) 762 to demonstrate that the knowledge of the oxide film and interface structure is of central importance for the study of oxide functionalities in general. For space limitations, we have confined ourselves to three examples, which we believe are representative for both the general themes we were investigating during the whole period and the collaboration between us and other experimental and theoretical groups.^[14–17] Some other important studies conducted in the context of SFB have been published in previous publications.^[18–25]

This Feature Article is organized as follows: in the following section, the basic principles of X-ray diffraction (XRD) are outlined to discuss its peculiarities when applied to 2D systems. In the following sections, the most important results related to the aforementioned different topics (1) oxidic AP, 2) multiferroic interface, and 3) 2DEG system are presented and discussed.

2. X-Ray Structure Analysis Applied to Surfaces

Although XRD is not a technique with an intrinsic sensitivity to surface or ultrathin films like low electron diffraction (LEED), today's highly brilliant synchrotron and in-house laboratory X-ray sources and modern data collection techniques allow the routine recording of diffracted intensities scattered by a submonolayer amount of a low-Z adsorbate like oxygen. We begin with a short summary of the most important peculiarities of SXRD as far it is necessary for the understanding of the data and results presented in this article. For more details, we refer to several reviews.^[26–29]

To outline the fundamental properties of XRD in the 2D limit, as shown in **Figure 1a**, a schematic of the reciprocal space in an a^*-c^* section is shown. On the right side, the corresponding crystal structure is given. Here, the crystal is “semi-infinite” along the c axis. As a result of the termination of the crystal, rods normal to the sample surface along the c^* axis in reciprocal space appear, which are shown as thin yellow solid lines. These rods are referred to as “crystal truncation rods” (CTRs), indicating that between the bulk Bragg points (solid dots), a diffuse rod of intensity exists, which originates from the truncation of the crystal, i.e., from the crystal's surface. In the a^*-b^* plane, they appear at integer positions (h, k) . The CTRs were theoretically predicted by Laue^[31] (Stacheliger Auswuchs), but it took until 1986 for a complete collection of CTR intensities by Robinson^[32] using synchrotron radiation. The intensity dynamics between the bulk Bragg reflections located at integer ℓ and the CTR intensity at the antiphase condition half way between the Bragg reflections amounts to about five orders of magnitude. The detailed calculation for an face-centered cubic-type crystal shows that at the antiphase condition, the intensity is equal to that of a quarter of a monolayer of the corresponding material. In consequence, adsorption of foreign species even in a submonolayer amount substantially modifies the total reflected intensity, which is a prerequisite for a meaningful analysis.

In the case of a primitive and semi-infinite crystal, the structure factor amplitude is given by the sum over the scattering contribution of all lattice planes (indexed by n), i.e., the sum extends from $n = -\infty$ to 0



Katayoon Mohseni graduated from the University of Tehran in Tehran (Iran) in 1988 in chemistry. She completed her doctorate in geochemistry at the Karlsruhe Institute of Technology (KIT) in 2007. Since 2007, she has been working at the Max-Planck Institute for Mikrostrukturphysik in Halle (Germany).



Holger Meyerheim graduated from the Ludwig-Maximilians-Universität (LMU) in Munich (Germany) in 1985 in mineralogy and crystallography. He completed his doctorate in experimental physics at the Freie Universität, Berlin, in 1990. In 1990, he moved to LMU to become Wissenschaftlicher Assistent where he established the SXRD group at the Institut für Kristallographie & Mineralogie. In 1995, he completed his “Habilitation”. In 1999, he joined the Max-Planck Institut für Mikrostrukturphysik in Halle (Germany), where he is group leader and “Privatdozent” at the Martin-Luther University Halle-Wittenberg.

$$F_{\text{CTR}} = \sum_{n=-\infty}^0 f \times \exp[2i\pi\ell n] \times g(h) \times g(k) \quad (1)$$

with the result using the geometric series $\sum x^n = 1/(1-x)$

$$F_{\text{CTR}} = \frac{f}{1 - \exp[-i2\pi\ell]} \times g(h) \times g(k) \quad (2)$$

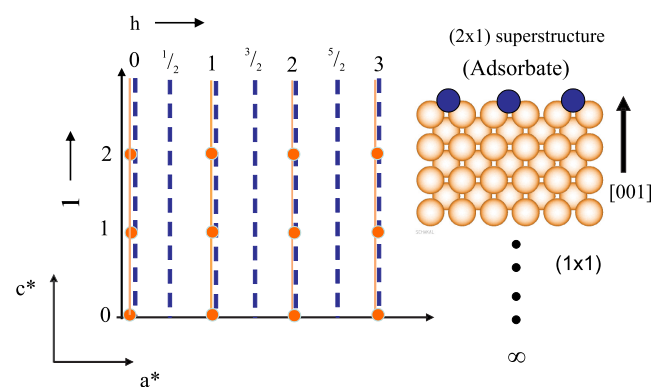


Figure 1. Schematic of the reciprocal space in an a^*-c^* section (left). The corresponding crystal structure is shown on the right. Bulk Bragg reflections of the semi-infinite crystal are represented as spheres at integer positions h and ℓ . The truncation of the crystal gives rise to rods along c^* (solid lines). Adsorption of foreign atoms at lattice sites involves a coherent summation of the scattering amplitudes between the rods of the substrate and those of the adsorbate, the latter represented by the dashed lines. In the case of a superstructure, here with a doubled periodicity along the a axis, extra rods appear at half-order positions along a^* . Reproduced with permission.^[30] Copyright 2017, Wiley-VCH.

with the atomic scattering amplitude (f) of the monoatomic substrate material. The functions $g(h)$ and $g(k)$ are the “Laue factors”^[31] along a^* and b^* (e.g., $[\sin(N_a\pi h)/\sin(\pi h)]$ along a^*), which in the case of an infinite crystal (e.g., $N_a \rightarrow \infty$) is equal to delta functions. The most important ingredient for the analysis of adlayers and interfaces is that adsorption of adatoms or relaxations of the substrate can be calculated by the coherent summation of the substrate-scattering amplitude (F_{CTR}) and the adsorbate amplitude. This leads to the total scattering amplitude (F_{tot}) expressed by

$$F_{\text{tot}} = F_{\text{CTR}} + \sum_j f_{\text{ad},j} \times \theta_j \times \exp[i2\pi(hx_j + ky_j + \ell z_j)] \quad (3)$$

where, $f_{\text{ad},j}$ represents the atomic scattering factor of the adsorbate and θ_j its fractional coverage. The summation index (j) indicates that the summation runs over all atoms of the adsorbate layer within the surface unit cell. In the case of an incommensurate adlayer, where no interference between the substrate and adlayer exists, only the scattering amplitude of the adlayer is recorded, yielding the structure information of the adlayer only. In the example shown in Figure 1, it is assumed that the adlayer forms a (2×1) superstructure with respect to the substrate, which leads to the appearance of fractional (half) order rods, which are also isolated from the CTRs. Recording reflected intensities along the CTRs and/or along the isolated superlattice (SL) rods is the basis of the surface structure determination by SXRD. We emphasize that surface sensitivity is achieved only by means of this “Fourier filtering” technique in k -space and has no relation with the frequently used experimental condition of “grazing incidence” of the incoming beam. In many experiments, the total external reflection condition is chosen where the beam is incident on the sample surface under the critical incidence angle ($\alpha_c \approx 0.3^\circ$ for Cu-K α radiation). This geometry is favorable to reduce to diffuse background due to thermal diffuse scattering from the bulk, but even under this condition, the decay length of the X-ray beam into the crystal is of the order of 10 nm, which cannot be seen as “surface sensitive” in the context of the studies discussed in the following paragraphs.

3. The AP of the 2D Oxidic QC

QCs have been first discovered in 1984^[11] and those that were synthesized in the following years were almost exclusively composed of metallic alloys. For an overview, e.g., refer the book of Steurer and Deloudi.^[33] Only recently an oxidic QC (OQC) was discovered which was grown on a Pt(111) surface.^[12] It exhibits a highly ordered 2D structure with a 12-fold (dodecagonal) rotation symmetry. Apart from the OQC, there exists an AP to the OQC whose atomic structure bears many resemblances to the OQC structure, as is shown in Figure 2. In the upper panels (a) and (b), the STM images of the OQC and the AP are compared with the tilings highlighted. As will be explained in the following sections, the bright spots representing apparent protrusions originate from titanium atoms. The difference between the OQC and the AP is that 30° rhombs appear in the OQC only. Here, the titanium atoms are arranged on the Stampfli–Gähler tiling.^[34,35] The red square in Figure 2b shows the unit cell of the AP (plane

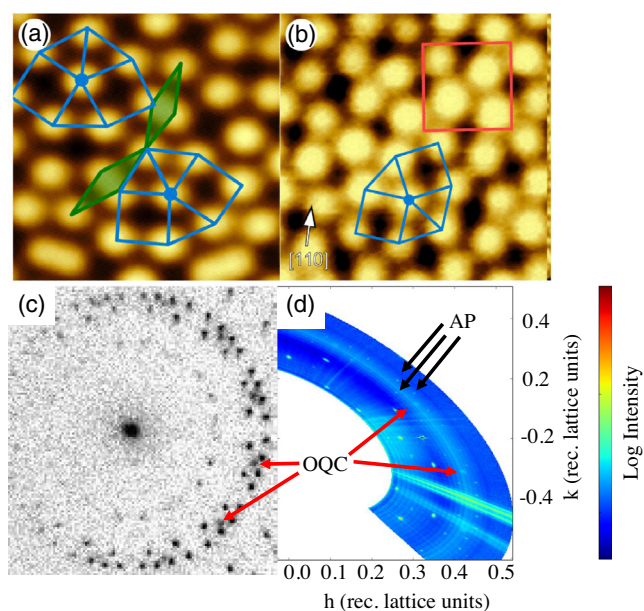


Figure 2. STM images of the a) OQC and its b) AP. STM parameters for OQC = $4 \times 4 \text{ nm}^2$, $I = 0.3 \text{ nA}$, $U = 1.0 \text{ V}$, for AP = $3.5 \times 3.5 \text{ nm}^2$, $I = 30 \text{ pA}$, $U = 0.1 \text{ V}$. The building block of the Kepler tiling common to both structures is emphasized by the blue squares and triangles. In (a), the rhombs which occur only in the OQC structure are highlighted (green). The red square in (b) indicates the unit cell used for the structure analysis of the AP. c) Experimental ($E = 20 \text{ eV}$) LEED pattern of the AP and the OQC which appears simultaneously. d) XRD spots of the AP and OQC. Some spots are indicated by the arrows. Reproduced with permission.^[13] Copyright 2016, American Physical Society.

group p2), with lattice parameters of $a_0 = 13.1 \text{ \AA}$, $b_0 = 12.9 \text{ \AA}$, and $\gamma = 90.5^\circ$. The AP tiling is the $3^2.4.3.4$ Archimedean tiling described by Kepler exactly 400 years ago.^[36] The lower panels (c) and (d) show the LEED and the SXRD patterns of a sample where both the OQC and the AP simultaneously exist. Some spots are labeled by “OQC” and “AP,” respectively.

SXRD experiments to analyze the atomic structure of the AP were conducted at the beamline ID03 of the European Synchrotron Radiation Facility (ESRF) in Grenoble (France). In total, 43 symmetry-independent in-plane reflection structure factor intensities ($|F_{\text{obs}}(hk0)|^2$) were collected by transverse φ scans about the surface normal under total reflection conditions of the incoming beam ($\lambda = 1.10 \text{ \AA}$). The 1σ uncertainty was estimated on the basis of the quadrature sum of the statistical uncertainty and the reproducibility of symmetry-equivalent reflections (systematic uncertainty). On average, we find 1σ to be equal to about 15%.

The data analysis was conducted in a classic way using the conventional Fourier techniques beginning with the calculation of the (z -projected) Patterson function, $P(u,v)$, providing information regarding the interatomic vectors within the unit cell.^[14,37] As the STM image provides information regarding the approximate titanium positions, a structure model can be set up quickly including the titanium atoms at the Kepler tiling positions. The Fourier synthesis of the charge density $[\rho(x,y)]$ which is given by $\rho(x,y) = \sum_{h,k} |F_{\text{obs}}(hk)| \times \exp[i\alpha_{\text{calc}}(hk)] \times \exp[-i2\pi(hx + ky)]$ ^[37]

provides the positions of both titanium and the heavy barium atoms. Refinement of the barium and titanium positions yields an unweighted residuum (R_U) of $R_U = 18\%$, ($R_U = \sum \|F_{\text{obs}}\| - |F_{\text{calc}}| / \sum |F_{\text{obs}}|$. Here, F_{obs} and F_{calc} are the experimental and calculated structure factors, respectively. The summation runs over all data points.) which is reasonably good to allow the interpretation that the structure model is basically correct. Using this model, $\rho(x,y)$ is again calculated, which is shown in **Figure 3**, together with the finally refined positions of the atoms. For a better visualization of the structure, four unit cells are shown.

Despite the fact that they were so far not included into the structure model, the oxygen atoms appear in $\rho(x,y)$ as faint contours directly proving their contribution to the AP structure. This is because the scattering phases [$\alpha_{\text{calc}}(hk)$, here either 0 or π] calculated with the model including barium and titanium only are correct, whereas the amplitudes [$|F_{\text{obs}}(hk)|$] are taken from the experiment. The oxygen positions could be refined, yielding an optimum residuum of $R_U \approx 14\%$. The tiling consists of two types of double triangles as well as of two types of slightly distorted squares in which barium atoms are located in the interior near the edges. Three oxygen atoms are arranged at the corners of a distorted triangle centered around the titanium atoms at an average distance of 2.14 Å (uncertainty for the Ti—O distance at about 0.1–0.2 Å).

The full analysis including the site occupancy factors yields a stoichiometry which can be written as $\text{Ba}_4\text{Ti}_4\text{O}_{10}$. Thus, the AP is

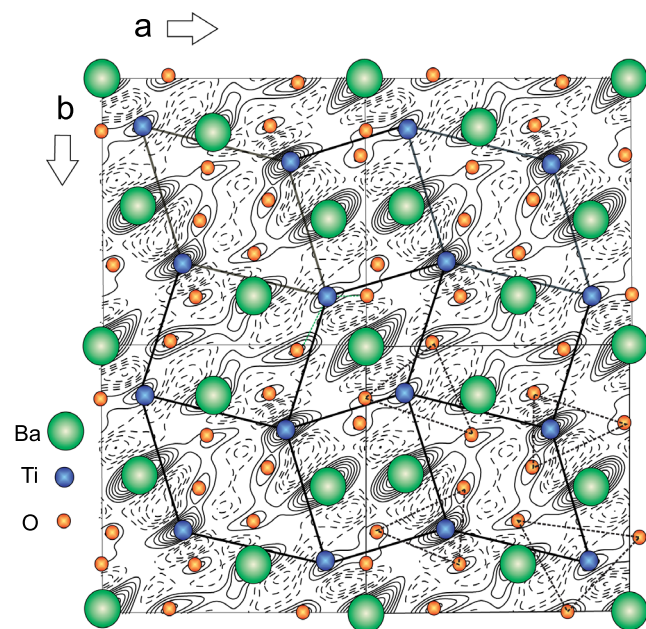


Figure 3. Structure model for the OQC AP with atomic sites (colored spheres, see left) superimposed over the calculated charge density contour plot [$\rho(x,y)$]. Four unit cells are shown. Titanium atoms (blue) are arranged in the Kepler-type tiling as indicated by the solid lines. Barium atoms (green) are located near the edges in the interior of the distorted squares. In the lower right, the threefold coordination of oxygen atoms (red) about titanium atoms is emphasized by dashed triangles. Reproduced with permission.^[13] Copyright 2016, American Physical Society.

characterized by oxygen deficiency as compared with BTO, which is in agreement with the oxygen-deficient preparation of the AP by annealing under ultrahigh vacuum (UHV) conditions and the fact that X-ray photoemission spectra indicate the presence of Ti^{3+} .^[12]

In summary, the SXRD analysis of the 2D structure of the AP has evidenced that the Kepler tiling positions are occupied by titanium atoms which were imaged by STM previously. This tiling has been discussed almost 400 years ago by Kepler and can be viewed as the oldest complex surface structure in history. The close resemblance between the AP and the corresponding OQC related to BTO is important to finally solve the structure of the OQC completely. Until now, the structure of the OQC is not completely known as it contains 30° rhombs which do not exist in the AP. We note that an SXRD structure analysis of the more complex STO-type AP to the corresponding OQC is in progress which also includes the presence of 30° rhombs. Here, it is by now evident that the rhombs do not contain any alkaline Earth element.^[38]

4. Atomic Structure of the Multiferroic Interface BTO/ME(001) (ME = Fe, Pd, Pt)

The functionality of a magnetic tunnel junction can be significantly extended when its insulating barrier is replaced by a ferroelectric. Apart from tunneling magnetoresistance (TMR), which is detected by switching the electrode magnetization from parallel ($\uparrow\uparrow$) to antiparallel ($\downarrow\uparrow$), the ferroelectric tunnel junction (FTJ) exhibits tunneling electro-resistance, seen upon the electric polarization reversal. Therefore, the FTJ resistance takes four different values, leading to a nonvolatile four-state memory device.^[2,3]

In consequence, the ME–oxide interface is at the heart of the development of novel oxide functional multiferroic devices, in which the barrier between the metallic electrodes is composed of a ferroelectric material. It is also desirable to intentionally modify the structure of the ME/oxide interface and with it its electronic transport properties, which are known to sensitively depend on the atomic structure as well as on the presence or absence of impurities. One prominent example is the TMR system Fe/MgO/Fe(001), which has been thoroughly investigated, both experimentally and theoretically,^[39–41] and which showed that oxygen impurities at the interface can greatly reduce the TMR.

In the context of the prototype perovskite-type ferroelectric BTO, first experimental studies have given evidence that ultrathin BTO layers can be grown on Fe(001)^[15] and vice versa,^[42] leading to well-defined coherent interfaces essential for ballistic tunneling. At the beginning of the research, calculations for the perovskite-type BTO barrier^[4–6] generally assumed symmetric structures with identical TiO_2 termination layers at the interface to the ME electrodes, an assumption which has been proven as over simplified due to the fact that BTO films grow in complete unit cells on the Fe(001) surface.^[15] In view of this observation, the structure investigation continued with a systematic study of the BTO/ME(001) interface, in which as MEs iron, palladium, and platinum were chosen. All three ME substrates provide good lattice matching conditions to BTO ($a = 3.991 \text{ \AA}$) as follows: 1) Fe(001) $\epsilon = +1.7\%$,

2) Pt(001) $\varepsilon = -1.8\%$, and 3) Pd(001) $\varepsilon = -2.5\%$. These values are related to the centered settings of the ME surface unit cells.

The ultrathin BTO films were grown in situ on the (001) surface of the different single-crystalline ME substrates by pulsed laser deposition (PLD) using a stoichiometric BTO target. The deposition was followed by annealing up to 550°C to obtain a long-range-ordered film structure. After preparation, the samples were transferred without breaking the UHV conditions to the six-circle X-ray diffractometer installed at the beamline ID32 of the European Synchrotron Radiation Facility (ESRF) in Grenoble (France).

As an example, symbols in **Figure 4** show the experimental structure factor magnitudes ($|F_{\text{abs}}(hkl)|$) collected for BTO/Pd(001)

long three CTRs [10ℓ , 11ℓ , and 20ℓ] as well as along several SL rods. Both types of rods appear as BTO forms a $c(2 \times 2)$ superstructure on the ME(001) surfaces involving rods of the adlayer being separated from the “integer order” CTRs of the substrate, as shown in Figure 1. Note the different scales along the ordinate used for the CTRs and the SLs. Black lines represent the fit to the data which is very good for all data sets (not shown here). The resulting structure models are discussed with the help of **Figure 5**.

Figure 5 shows the comparison of the structure models derived from the SXRD analysis. We have investigated four different samples: 1) BTO/Fe(001), 2) BTO/Fe(001)_(c), 3) BTO/Pd(001), and 4) BTO/Pt(001). Figure 5b shows the sample where

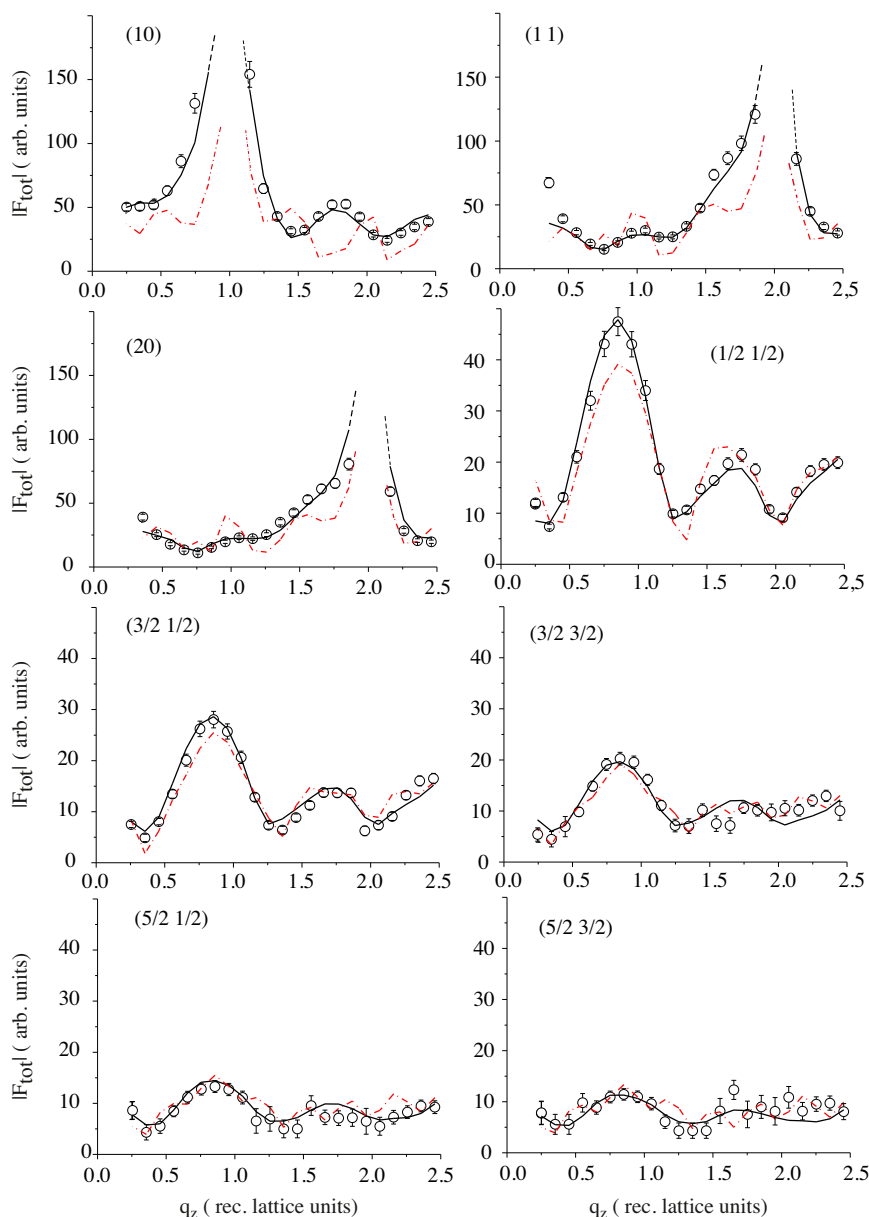


Figure 4. Experimental (symbols) and calculated (lines) structure factor amplitudes for BTO on Pd(001). Note the different y-axis scales for SL rods (half order) and CTRs (integer order). Solid (black) and dashed (red) lines correspond to calculated $|F_{\text{tot}}|$ s assuming a TiO_2 and a BaO layer at the interface to Pd(001) (see text). Reproduced with permission.^[16] Copyright 2013, American Physical Society.

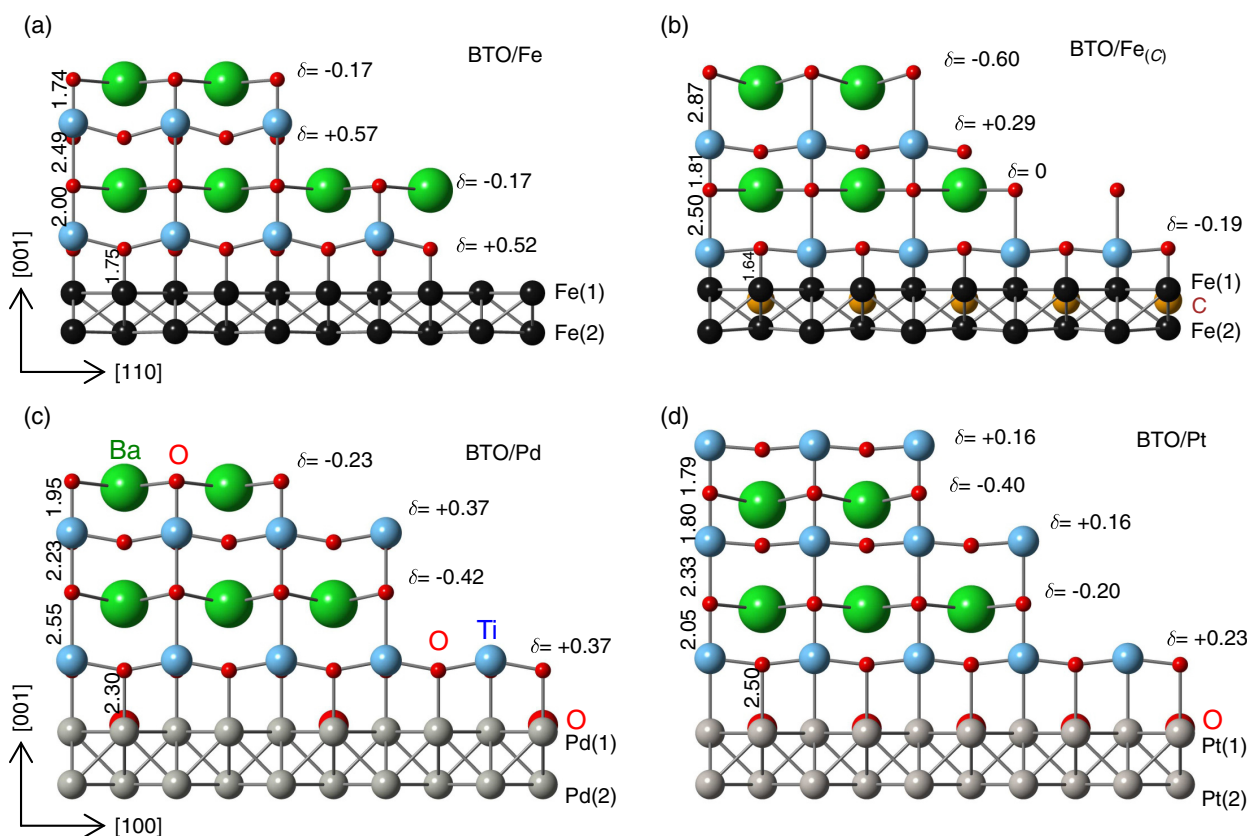


Figure 5. SXR-derivated structure models for ultrathin BTO films grown on ME substrates: a) BTO/Fe, b) BTO/Fe_(c), c) BTO/Pd, and d) BTO/Pt. Oxygen, barium, and titanium atoms are represented by small- (red), large- (green), and medium-sized (blue) spheres. Interatomic distances vertical relaxations (δ) of the cations relative to the oxygen atoms are given in Ångström units. Fractional coverage of a layer is quantitatively represented by the number of spheres in the layers relative to that in the substrate. Reproduced with permission.^[16] Copyright 2013, American Physical Society.

prior to BTO deposition, the Fe(001) surface was dosed by carbon to form a $c(2 \times 2)$ superstructure indicative of carbon “contamination” on the surface. The fractional coverage of the layers is approximately represented by the number of spheres. For all samples, we have chosen a film thickness where two BTO unit cells cover the ME(001) surface by a fraction of at least 50%.

The most important result of this study is the observed inversion of the film/vacuum termination layer from pure BaO in the case of BTO/Fe(001) to pure TiO₂ in the case of BTO/Pt(001), whereas a mixed situation (BaO and TiO₂ termination) is encountered for BTO/Pd(001). By contrast, the interface to the ME surface is always terminated by a TiO₂ layer with a ME—oxygen bond distance increasing from 1.75 Å (Fe) via 2.30 Å (Pd) to 2.50 Å (Pt). The stability of the ME/TiO₂ interface configuration has been confirmed by first-principles calculations.^[16,43] The inversion of the layer termination can be traced back to the condition of charge neutrality. It goes in parallel with the increasing concentration of impurities (oxygen, carbon) at the BTO/ME interface, whereas it is zero in the case of the Fe(001) surface; the concentration of oxygen atoms residing in surface fourfold hollow sites increases to about 25% of a monolayer in the case of the Pd(001) surface (c) and to 50% of a monolayer for Pt(001) (d). Correspondingly, the BTO film grown on the carbon contaminated Fe(001) surface (b) also has a mixed TiO₂/BaO film termination.

We emphasize that the experimental evidence for the correctness of the different structure models is very strong. For instance, the red dashed lines in Figure 4 show the calculated $|F(hk\ell)|$, assuming a BaO layer at the interface to the Pd(001) surface which on the basis of the fit quality can be clearly ruled out. For instance, the black line corresponds to a fit with $R_U \approx 10\%$ and a goodness of fit (GOF) ($R_U = \sum ||F_{\text{obs}}| - |F_{\text{calc}}|| / \sum |F_{\text{obs}}|$. Here, F_{obs} and F_{calc} are the experimental and calculated structure factors, respectively. The summation runs over all datapoints. The GOF is given by: $\text{GOF} = \sqrt{1/(N - P) \cdot \sum [(I_{\text{obs}} - I_{\text{calc}})^2 / \sigma^2]}$, where the difference between observed and calculated intensities is normalized to the uncertainties expressed by the standard deviation (σ) and to $(N - P)$, i.e., the difference between the number of independent data points (N) and the number of parameters (P) which are varied.), whereas the red line corresponds to a fit with R_U being in the 30–40% range (GOF = 4.8).

The different interfaces and film structures affect the electronic properties. To study these, the z -resolved charge density $[\rho(z)]$ at the Fermi level (E_F) was calculated using a self-consistent Green function method designed especially for semi-infinite layered systems.^[44] In Figure 6, $\rho(z)$ is shown after integration over the 2D unit cell. The presence of interfacial impurities in the case of BTO/Pd and BTO/Pt was considered and calculated for three

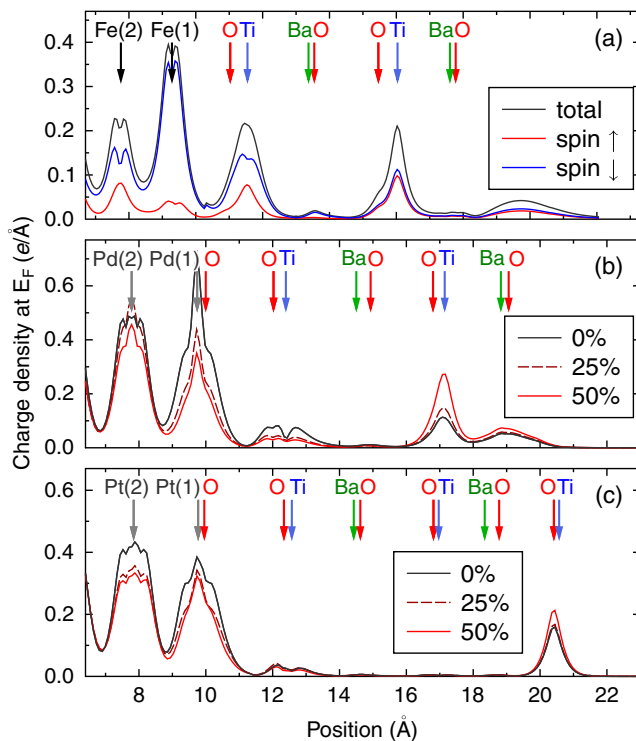


Figure 6. Z-resolved charge distribution calculated at the Fermi level for a) BTO/Fe, b) BTO/Pd, and c) BTO/Pt films. In the case of BTO/Fe, the spin-resolved and total charge distribution are shown, in the case of BTO/Pd and BTO/Pt, the different lines correspond to calculations assuming 0.00, 0.25, and 0.50 ML of oxygen at the interface (see labels). Arrows indicate the atomic positions taken from the structure analysis. Reproduced with permission.^[16] Copyright 2013, American Physical Society.

different occupancies (θ): $\theta = 0$ monolayer (ML) (pure case), $\theta = 0.25$ ML, and $\theta = 0.50$ ML.

The calculations indicate that the BTO film surface is metallic in all cases. The difference between the BaO and the TiO₂-terminated BTO film is that in the latter case $\rho(z)$ is more localized. In addition, at the TiO₂/Fe(001) interface, there is a spin polarization in which the charge density with a minority spin is dominant. There is also an enhancement of $\rho(z)$ due to the strong bonding between the oxygen atoms in the first TiO₂ layer and the Fe substrate (see Figure 6a). By contrast, both spin polarization (not shown) and enhancement of $\rho(z)$ are not observed for BTO/Pd(001) and BTO/Pt(001), as shown in Figure 6b,c. Finally, it is found that in the case of BTO/Pd and BTO/Pt, the presence of a partially filled oxygen layer at the ME/BTO interface has only a minor effect on $\rho(z)$, which allows the suggestion that the electronic transport via tunneling mediated by electronic states with Δ_1 symmetry is also hardly affected in this case. The Δ_1 states (p_z and d_{z^2} orbitals) are identified as states which are important for coherent transport.^[41,45,46]

5. Chemical Roughness at the LAO/STO Interface and Its Influence on the 2DEG Formation

One of the most important new functionalities that have been discovered in all-oxide systems is the formation of a 2DEG at

the interface between a polar and a nonpolar oxide. The archetype example is the combination between LAO and STO for which above a critical LaO film thickness of four unit cells the formation of the 2DEG sets in [7,47,48]. This metallization was explained by theory to be the result of the “polar catastrophe”^[8] induced by the electric field which increases with increasing LaO film thickness. Above a certain film thickness, the energy of the system is lowered by a charge transfer from the LAO surface to the interface to form the 2DEG.

In the following years, many different systems were found to exhibit the 2DEG formation, but there is still an ongoing discussion regarding the models for its appearance. For instance, oxygen off-stoichiometry as well as intermixing at the interface have been proposed to be important for 2DEG formation.^[9,10,49,50] Deviations from stoichiometry such as the presence of oxygen defects act as n-doping (favoring 2DEG formation), whereas cation intermixing might act as p-doping (inhibiting 2DEG formation). The role of such imperfections is complex and not known in detail. Based on thermodynamic arguments involving interface redox reactions the LaFeO₃ (LFO)/STO interface which is studied here was predicted to be insulating.^[51]

Thus, a precise structure analysis is required to draw conclusions regarding the driving mechanisms of the 2DEG formation. In this study, we have investigated the structure and electronic properties of thin LFO films grown, almost lattice matched (mismatch 0.53%) on differently prepared STO(001) substrates. As also confirmed by first-principles calculations discussed in the following paragraphs, this very low mismatch excludes different mechanisms such as strain-induced polarization which has been discussed recently as the origin for 2D conductance in nonpolar oxide heterostructures as found, e.g., in CaZrO₃/STO.^[52] In combination with ab initio calculations using the XRD-derived interface structure model, we show that both the presence of oxygen defects and the different degrees of cation intermixing at the interface strongly influence the 2DEG formation.^[17]

The LFO films were deposited on STO(001) substrates at 760 °C using oxygen plasma-assisted molecular beam epitaxy. The oxygen partial pressure was 4×10^{-7} mbar. The TiO₂-terminated STO substrate surface was initially cleaned using acetone, methanol, and deionized water, followed by dipping in 1:7 buffered hydrofluoric acid (BHF) with NH₄F. One sample was used as the substrate as prepared (type A surface), whereas a second one was subject to annealing at 1000 °C in oxygen flow at a partial oxygen pressure greater than 1 atm for 90 min (type B surface). For more details, we refer to the study by Xu et al.^[17] Figure 7a,b shows atomic force microscopy images recorded for samples (A) and (B), respectively. The surfaces are atomically smooth and characterized by steps of unit cell height (3.9 Å). The corresponding profiles along the white lines are shown in Figure 7c,d, respectively. Sample annealing as done for sample (B) leads to smooth straight step edges, whereas for sample (A) where only BHF etching was applied terraces and step edges exhibit a rougher morphology. The surface morphology of the subsequently grown LFO films is similar to that of the corresponding substrates.

The different sample preparation procedures are decisive for the electronic properties. The at-room-temperature sheet resistance as measured by the Van der Pauw method is shown in Figure 7e versus LFO film thickness. While LFO films grown

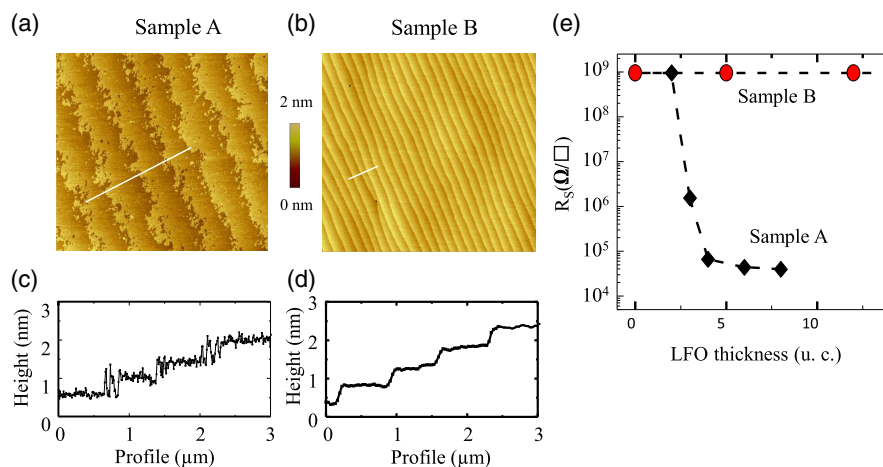


Figure 7. Atomic force microscopy images of a) the STO(001) surface recorded after BHF etching without subsequent annealing (type A substrate) and b) after BHF etching and annealing (type B substrate). The corresponding height profiles along the lines are shown in (c) and (d). e) LFO thickness-dependent room-temperature sheet resistance for sample (A) and (B). Adapted with permission.^[17] Copyright 2017, Wiley-VCH.

on type (B) STO are always insulating, those grown on type (A) substrates show a transition from the insulating ($t < 2$ u.c.) to metallic ($t > 4$ u.c.) behavior.

XRD experiments were conducted at the beamline ID03 of the European Synchrotron Radiation Facility (ESRF) in Grenoble (France) using a six circle diffractometer operated in the z -axis mode at grazing incidence ($\alpha_i = 2^\circ$) of the incoming beam (photon energy = 24 keV). Samples of type (A) and (B) with a LFO film of 6 u.c. thickness were investigated. Six symmetry-independent CTRs corresponding to ≈ 700 – 800 reflections in total were collected up to a maximum momentum transfer of $q_z = \ell \times c^* = 3.7$ reciprocal lattice units (RLU). One example is shown

in **Figure 8** for the metallic sample (A) in which symbols and lines correspond to experimental and calculated structure factor magnitudes ($|F(hk\ell)|$), respectively. The structure analysis was conducted by least squares refinement of the calculated $|F(hk\ell)|$ to the experimental ones using the program “Prometheus.”^[53]

The analysis benefits from the high $p4mm$ plane group symmetry of the sample structure which requires only the atomic z -parameters to be refined in addition to an overall Debye parameter describing static and dynamic disorder^[54] and the occupancy factors (θ) of the atomic species within each layer. The fit quality is given by $R_U = 0.15$ and $GOF = 1.8$, which can be considered as quite satisfactory. As shown in Figure 8,

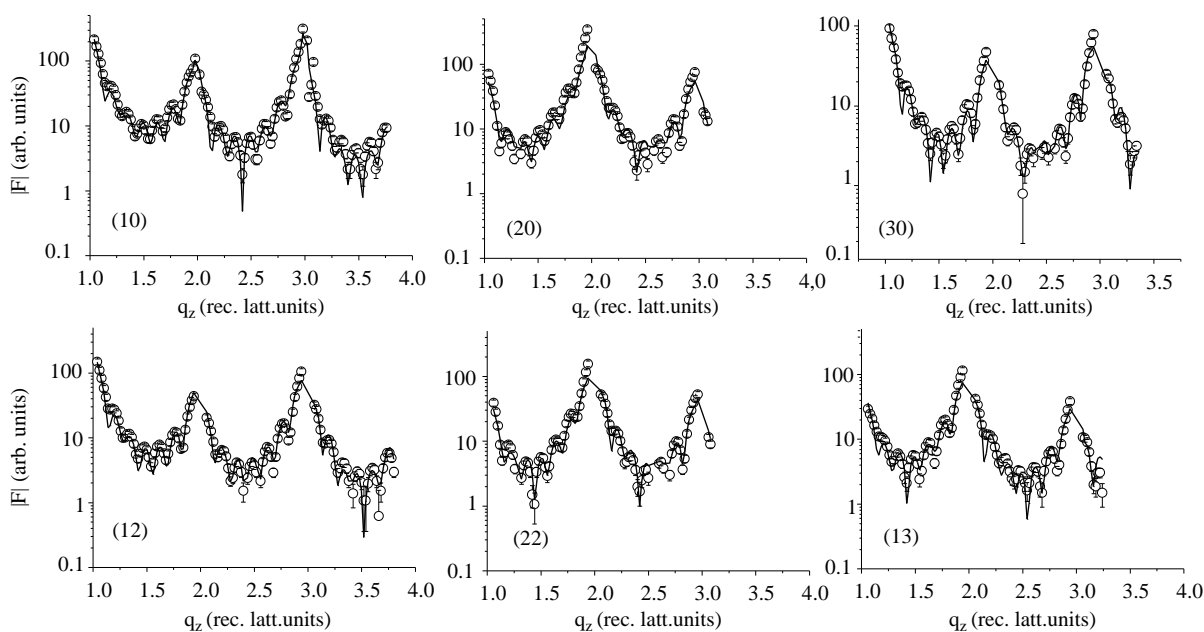


Figure 8. Experimental (symbols) and calculated (lines) structure factor amplitude along several symmetry-independent CTRs collected for the conducting sample.

the lines follow the experimental data points in all detail. Intensity oscillations (Laue fringes) are due to the finite LFO film thickness. Bulk Bragg reflections occur at integer values of ℓ but are omitted in the fitting of the data.

The most important result of the XRD analysis is that the conducting sample (A) is characterized by a lesser degree of cationic exchange (10% exchange of $\text{Sr}^{2+}/\text{La}^{3+}$ and 25% $\text{Fe}^{3+}/\text{Ti}^{4+}$) at the interface as compared with the insulating one (25% $\text{Sr}^{2+}/\text{La}^{3+}$ and 50% $\text{Fe}^{3+}/\text{Ti}^{4+}$). Structure models of the conducting and the insulating samples are shown in **Figure 9a,d**, respectively. The XRD analysis supports transmission electron microscopy

(TEM) experiments which have indicated different degrees of cationic exchange between samples (A) and (B).^[17]

Based on the structure models, first-principles calculations were performed to identify the effect of cationic exchange and oxygen off-stoichiometry on electric properties. It can be qualitatively concluded that cationic exchange tends to favor insulating behavior. This is confirmed by the calculated layer-resolved bandgap and the density of states (DOSs) which are shown in **Figure 9b,c,e,f**, respectively. It is found that sample A (less cationic exchange) is conducting, whereas sample B (enhanced cationic exchange) is insulating, which is in agreement with the

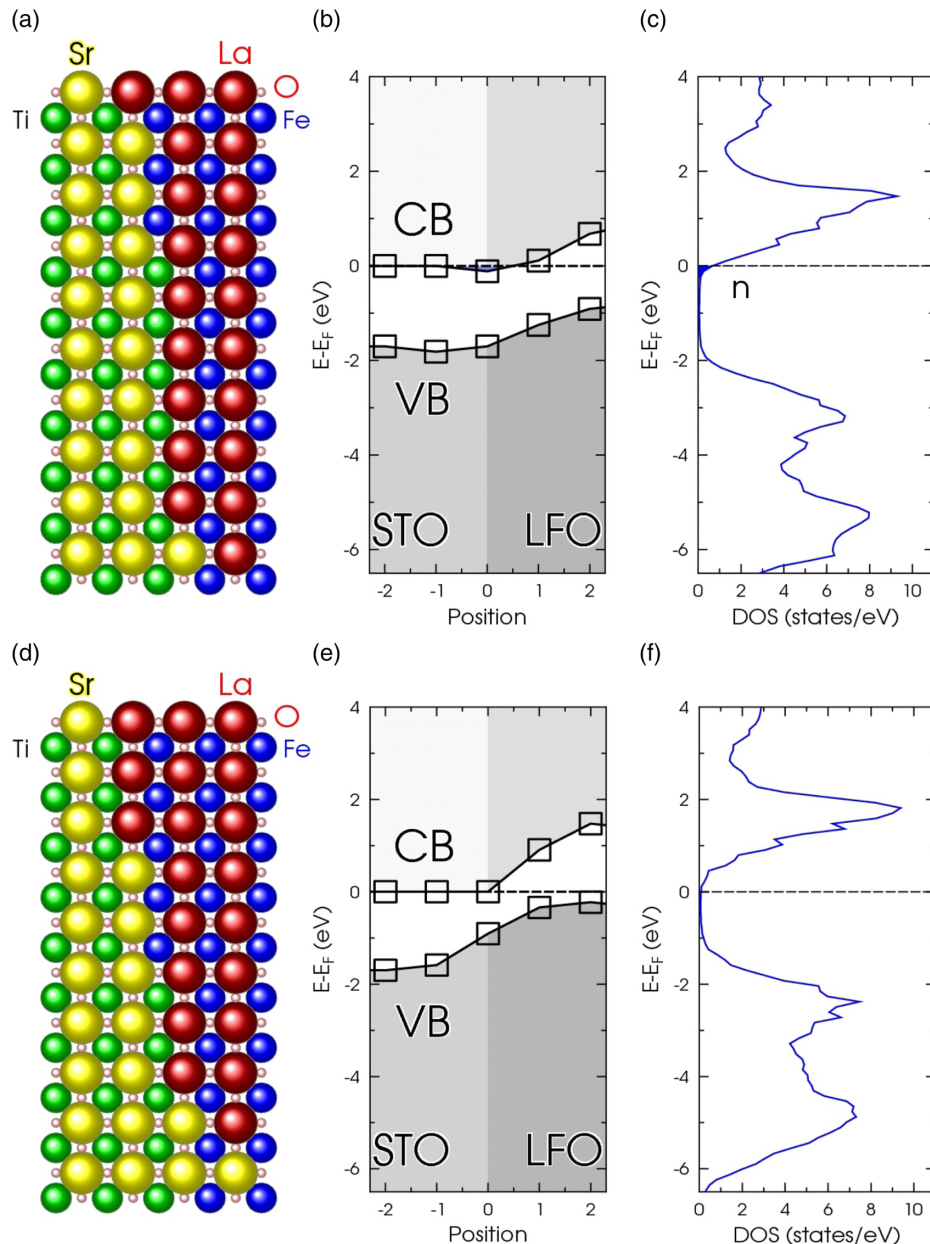


Figure 9. SXR-derived structure models, calculated-layer-resolved bandgaps, and DOSs for the metallic (upper panel) and the insulating sample (lower panel). Note that the degree of cation intermixing (Sr^{2+} vs La^{3+} and Fe^{3+} vs Ti^{4+}) at the STL/LFO interface is different. For the conducting sample, a 10% exchange of $\text{Sr}^{2+}/\text{La}^{3+}$ and 25% $\text{Fe}^{3+}/\text{Ti}^{4+}$ is determined, whereas for the insulating sample, a 25% $\text{Sr}^{2+}/\text{La}^{3+}$ and 50% $\text{Fe}^{3+}/\text{Ti}^{4+}$ exchange is found. Adapted with permission.^[17] Copyright 2017, Wiley-VCH.

experiment. The cationic exchange reduces the DOS near the Fermi level (E_F), which is equivalent to p-doping and which leads to the opening of a bandgap. This result is also in agreement with several previous investigations on LFO/STO^[55] and similar systems such as LaCrO₃,^[9] where cationic exchange was suggested to be responsible for the insulating behavior. In contrast, oxygen defects (not shown here) involve n-doping which favors 2DEG formation. In consequence, depending on the balance between oxygen defects and the degree of cationic exchange at the interface, the critical thickness for the sample to become conducting varies. For instance, a 2 u.c.-thick LFO film with a 10% La³⁺/Sr²⁺ exchange is insulating, whereas it becomes conducting at a thickness of 4 u.c., although the width of the DOS at E_F becomes smaller than that in the perfect interface case.^[17] This is in agreement with the experimental evidence that there is no 2DEG at an LFO thickness of 3 u.c. (see Figure 7), which is attributed to cation intermixing (sample A).

6. Conclusions

In this Feature Article, we have presented three studies which were conducted during the SFB 762 (functionality of oxide interfaces). We have demonstrated that the precise XRD structure analysis of very complex oxide films and interfaces is a prerequisite for understanding their functionality. The unique combination of the XRD-derived structure information with ab initio calculations (using the atomic coordinates as input) on the one hand and with different experimental techniques (e.g., STM, TEM, etc.) on the other has yielded deep insights into the correlation between the physical properties and subtle details of the film and interface structures. Examples are the onset of the 2DEG-induced conductance at the LFO/STO interface and the influence of interface impurities (oxygen, carbon) at the BTO/ME interface on the resulting film structure and termination. Finally, our SXRD analysis of the AP to the oxidic BTO-derived 2D dodecagonal QC has independently proven the involvement of oxygen into the structure. We note that this study was the first step of subsequent studies on more complex systems (e.g., STO), which allowed to solve the structure of the corresponding QC.

Acknowledgements

This work was supported by the Deutsche Forschungsgemeinschaft (DFG) through SFB 762 (functionality of oxide interfaces). The authors thank Arthur Ernst, Ingrid Mertig, Wolf Widdra, Stefan Förster, Igor Maznichenko, Sergei Ostanin, Dirk Sander, Sumalay Roy, Andrey Polyakov, Nathalie Jedrecy, German Castro, Roberto Felici, Jörg Zegenhagen, and Juan Rubuio-Zuazo for their collaboration. Technical help by Frank Weiß is gratefully acknowledged. H.L.M. and K.M. also thank the staff of ESRF for their hospitality and support during their visits in Grenoble. The authors thank Stuart S.P. Parkin and Jürgen Kirschner for their support and scientific discussions.

Conflict of Interest

The authors declare no conflict of interest.

Keywords

Kepler approximants, multiferroic interfaces, surface X-ray diffraction, 2D electron gases

Received: September 25, 2019

Revised: November 7, 2019

Published online: December 4, 2019

- [1] M. Lorenz, M. Rao, T. Venkatesan, E. Fortunato, P. Barquinha, R. Branquinho, D. Salgueiro, R. Martins, E. Carlos, A. Liu, F. Shan, M. Grundmann, H. Boschker, J. Mukherjee, P. Dm, N. DasGupta, D. Rogers, F. H. Teherani, E. Sandana, N. Pryd, *J. Phys. D Appl. Phys.* **2016**, *49*, 433001.
- [2] J. P. Velev, C. G. Duan, J. D. Burton, A. Smogunov, M. K. Niranjana, E. Tosatti, S. S. Jaswal, E. Y. Tsymbal, *Nano Lett.* **2009**, *9*, 427.
- [3] V. Garcia, M. Bibes, L. Bocher, S. Valencia, F. Kronast, A. Crassous, X. Moya, S. Enouz-Vedrenne, A. Gloter, D. Imhoff, C. Deranlot, N. D. Mathur, S. Fusil, K. Bouzehouane, A. Barthelemy, *Science* **2010**, *327*, 1106.
- [4] J. P. Velev, C. G. Duan, K. D. Belashchenko, S. S. Jaswal, E. Y. Tsymbal, *Phys. Rev. Lett.* **2007**, *98*, 137201.
- [5] J. P. Velev, C. G. Duan, K. D. Belashchenko, S. S. Jaswal, E. Y. Tsymbal, *J. Appl. Phys.* **2008**, *103*, 07A701.
- [6] M. Stengel, D. Vanderbilt, N. A. Spaldin, *Nat. Mater.* **2009**, *8*, 392.
- [7] A. Ohtomo, H. Y. Hwang, *Nature* **2004**, *427*, 423.
- [8] S. Okamoto, A. J. Millis, *Group* **2004**, *428*, 630.
- [9] L. Qiao, T. Droubay, T. Kaspar, P. Sushko, S. Chambers, *Surf. Sci.* **2011**, *605*, 1381.
- [10] J. N. Eckstein, *Nat. Mater.* **2007**, *6*, 473.
- [11] D. Shechtman, I. Blech, D. Gratias, J. W. Cahn, *Phys. Rev. Lett.* **1984**, *53*, 1951.
- [12] S. Förster, K. Meinel, R. Hammer, M. Trautmann, W. Widdra, *Nature* **2013**, *502*, 215.
- [13] S. Förster, M. Trautmann, S. Roy, W. A. Adeagbo, E. M. Zollner, R. Hammer, F. O. Schumann, K. Meinel, S. K. Nayak, K. Mohseni, W. Hergert, H. L. Meyerheim, W. Widdra, *Phys. Rev. Lett.* **2016**, *117*, 095501.
- [14] S. Roy, K. Mohseni, S. Förster, M. Trautmann, F. Schumann, E. Zollner, H. Meyerheim, W. Widdra, Z. Krist, *Zeitschrift für Kristallographie Cryst. Mater.* **2016**, *231*, 749.
- [15] H. L. Meyerheim, F. Klimenta, A. Ernst, K. Mohseni, S. Ostanin, M. Fechner, S. Parihar, I. V. Maznichenko, I. Mertig, J. Kirschner, *Phys. Rev. Lett.* **2011**, *106*, 087203.
- [16] H. L. Meyerheim, A. Ernst, K. Mohseni, I. V. Maznichenko, J. Henk, S. Ostanin, N. Jedrecy, F. Klimenta, J. Zegenhagen, C. Schlueter, I. Mertig, J. Kirschner, *Phys. Rev. Lett.* **2013**, *111*, 105501.
- [17] P. Xu, W. Han, P. M. Rice, J. Jeong, M. G. Samant, K. Mohseni, H. L. Meyerheim, S. Ostanin, I. V. Maznichenko, I. Mertig, E. K. U. Gross, A. Ernst, S. S. P. Parkin, *Adv. Mater.* **2017**, *29*, 1604447.
- [18] C. Tusche, H. L. Meyerheim, J. Kirschner, *Phys. Rev. Lett.* **2007**, *99*, 026102.
- [19] H. L. Meyerheim, C. Tusche, A. Ernst, S. Ostanin, I. V. Maznichenko, K. Mohseni, N. Jedrecy, J. Zegenhagen, J. Roy, I. Mertig, J. Kirschner, *Phys. Rev. Lett.* **2009**, *102*, 156102.
- [20] S. S. Parihar, H. L. Meyerheim, K. Mohseni, S. Ostanin, A. Ernst, N. Jedrecy, R. Felici, J. Kirschner, *Phys. Rev. B* **2010**, *81*, 075428.
- [21] H. L. Meyerheim, A. Ernst, K. Mohseni, I. V. Maznichenko, S. Ostanin, F. Klimenta, N. Jedrecy, W. Feng, I. Mertig, R. Felici, J. Kirschner, *Phys. Rev. Lett.* **2012**, *108*, 215502.
- [22] W. Feng, H. L. Meyerheim, K. Mohseni, O. Brovko, V. S. Stepanyuk, N. Jedrecy, R. Felici, J. Kirschner, *Phys. Rev. Lett.* **2013**, *110*, 235503.

- [23] S. Roy, H. L. Meyerheim, K. Mohseni, Z. Tian, D. Sander, M. Hoffmann, W. Adeagbo, A. Ernst, W. Hergert, R. Felici, J. Kirschner, *Phys. Rev. B* **2014**, *89*, 165428.
- [24] H. L. Meyerheim, A. Ernst, K. Mohseni, C. Tusche, W. A. Adeagbo, I. V. Maznichenko, W. Hergert, G. R. Castro, J. Rubio-Zuazo, A. Morgante, N. Jedrecy, I. Mertig, J. Kirschner, *Phys. Rev. B* **2014**, *90*, 085423.
- [25] O. O. Brovko, D. I. Bazhanov, H. L. Meyerheim, D. Sander, V. S. Stepanyuk, J. Kirschner, *Surf. Sci. Rep.* **2014**, *69*, 159.
- [26] E. Vlieg, J. V. D. Veen, S. Gurman, C. Norris, J. Macdonald, *Surf. Sci.* **1989**, *210*, 301.
- [27] I. K. Robinson, *Handbook on Synchrotron Radiation*, Vol. 3, North Holland, Amsterdam **1991**, Ch. 7.
- [28] I. K. Robinson, D. J. Tweet, *Rep. Prog. Phys.* **1992**, *55*, 599.
- [29] H. Meyerheim, W. Moritz, *Appl. Phys. A* **1998**, *67*, 645.
- [30] H. L. Meyerheim, C. Tusche, *Phys. Status Solidi RRL* **2018**, *12*, 1870337.
- [31] M. v. Laue, *Ann. d. Physik* **1936**, *26*, 55.
- [32] I. Robinson, *Phys. Rev. B* **1986**, *33*, 3830.
- [33] W. Steurer, S. Deloudi, *Crystallography of Quasicrystals*, Springer, Berlin **2009**.
- [34] P. Stampfli, *Helv. Phys. Acta.* **1986**, *59*, 1260.
- [35] F. Gähler, Proceedings of the I.L.L./Codest Workshop, World Scientific, Singapore **1988**.
- [36] J. Kepler, *Harmonices Mundi*, Linz, Austria **1619**.
- [37] M. J. Buerger, *Kristallographie. Eine Einführung in die geometrische und röntgenographische Kristallkunde*, Walter de Gruyter Verlag, Berlin **1977**.
- [38] unpublished.
- [39] H. L. Meyerheim, R. Popescu, J. Kirschner, N. Jedrecy, M. Sauvage-Simkin, B. Heinrich, R. Pinchaux, *Phys. Rev. Lett.* **2001**, *87*, 076102.
- [40] X. G. Zhang, W. H. Butler, A. Bandyopadhyay, *Phys. Rev. B* **2003**, *68*, 092402.
- [41] C. Tusche, H. L. Meyerheim, N. Jedrecy, G. Renaud, A. Ernst, J. Henk, P. Bruno, J. Kirschner, *Phys. Rev. Lett.* **2005**, *95*, 176101.
- [42] L. Bocher, A. Gloter, A. Crassous, V. Garcia, K. March, A. Zobelli, S. Valencia, S. Enouz-Vedrenne, X. Moya, N. D. Marthur, C. Deranlot, S. Fusil, K. Bouzehouane, M. Bibes, A. Barthélémy, C. Colliex, O. Stéphan, *Nano Lett.* **2012**, *12*, 376.
- [43] P. M. Deleuze, A. Mahmoud, B. Domenichini, C. Dupont, *Phys. Chem. Chem. Phys.* **2019**, *21*, 4367.
- [44] M. Lüders, A. Ernst, W. M. Temmerman, Z. Szotek, P. J. Durham, *J. Phys. Condens. Matter* **2001**, *13*, 8587.
- [45] C. Tusche, H. L. Meyerheim, N. Jedrecy, G. Renaud, A. Ernst, J. Henk, P. Bruno, C. J. Kirschner, *Phys. Rev. Lett.* **2006**, *96*, 119602.
- [46] P. Bose, P. Zahn, I. Mertig, J. Henk, *Phys. Rev. B* **2011**, *83*, 174451.
- [47] S. Thiel, G. Hammerl, A. Schmehl, C. W. Schneider, J. Mannhart, *Science* **2006**, *313*, 1942.
- [48] C. Cen, S. Thiel, J. Mannhart, J. Levy, *Science* **2009**, *323*, 1026.
- [49] G. Herranz, M. Basleti c., M. Bibes, C. Carrétéro, E. Tafra, E. Jacquet, K. Bouzehouane, C. Deranlot, A. Hamzi c, J. M. Broto, A. Barthélémy, A. Fert, *Phys. Rev. Lett.* **2007**, *98*, 216803.
- [50] Z. Q. Liu, C. J. Li, W. M. Lü, X. H. Huang, Z. Huang, S. W. Zeng, X. P. Qiu, L. S. Huang, A. Annadi, J. S. Chen, J. M. D. Coey, T. Venkatesan, Ariando, *Phys. Rev. X* **2013**, *3*, 021010.
- [51] Y. Chen, R. J. Green, *Adv. Mater. Interfaces* **2019**, *6*, 1900547.
- [52] Y. Chen, F. Trier, T. Kasama, D. V. Christensen, N. Bovet, Z. I. Balogh, H. Li, K. T. S. Thyden, W. Zhang, S. Yazdi, P. Norby, N. Pryds, S. Linderth, *Nano Lett.* **2015**, *15*, 1849.
- [53] U. H. Zucker, E. Perenthaler, W. F. Kuhs, R. Bachmann, H. Schulz, *J. Appl. Crystallogr.* **1983**, *16*, 358.
- [54] W. F. Kuhs, *Acta Cryst. A* **1992**, *48*, 80.
- [55] M. Nakamura, F. Kagawa, T. Tanigaki, H. S. Park, T. Matsuda, D. Shindo, Y. Tokura, M. Kawasaki, *Phys. Rev. Lett.* **2016**, *116*, 156801.